NANO LETTERS

2007
Vol. 7, No. 2
243−246

Few Electron Double Quantum Dots in InAs/InP Nanowire Heterostructures

Andreas Fuhrer,* Linus E. Fröberg, Jonas Nyvold Pedersen, Magnus W. Larsson, Andreas Wacker, Mats-Erik Pistol, and Lars Samuelson

The Nanometer Structure Consortium, Lund University, Box 118, S-221 00 Lund, Sweden

Received August 15, 2006; Revised Manuscript Received October 31, 2006

ABSTRACT

We report on fabrication of double quantum dots in catalytically grown InAs/InP nanowire heterostructures. In the few-electron regime, starting with both dots empty, our low-temperature transport measurements reveal a clear shell structure for sequential charging of the larger of the two dots with up to 12 electrons. The resonant current through the double dot is found to depend on the orbital coupling between states of different radial symmetry. The charging energies are well described by a capacitance model if next-neighbor capacitances are taken into account.

Carbon nanotubes[1,2] and nanowires[3,4] are potential candidates for future electronic building blocks such as planar metal-oxide-semiconductor field effect transistors[5,6] and highly integrated vertical electronic devices.[7,8] While selective and position-controlled growth of semiconducting carbon nanotubes remains problematic, it has been demonstrated that a high degree of control over position,[9] material composition,[10,11] and doping[12] is possible in semiconducting nanowires.

Heterostructures have been implemented for different material combinations both in radial direction[5,13,14] and along the axis of the nanowires.[10,15,16] Axial InP/InAs heterostructures have been used as double-barrier few-electron quantum dots, and tunability of the effective electron *g*-factor has been demonstrated.[17] Similarly, supperlattices have been proposed as memory cells with possible high-density vertical integration.[16] For the implementation of such electronic devices, it is imperative to have good control over the heterostructure growth and the electronic characteristics thereof. In the present study, we therefore investigate double quantum dot structures defined by three InP barriers in InAs nanowires and demonstrate control over barrier and dot size. We further analyze one of the devices in detail using electron transport measurements and show that a capacitance matrix approach gives quantitative agreement with the measured data. For an overview on double quantum dots in different material systems, we refer the reader to refs 18−23 and references therein.

InAs/InP nanowire heterostructures were grown using chemical beam epitaxy (CBE) on InAs (111)B substrates using size-selected gold aerosol nanoparticles as a catalyst.[24] Diameters of the wires were in the range of 40−50 nm, determined by the size distribution of the Au nanoparticles. In CBE, precursors are supplied in a molecular beam entering an ultrahigh vacuum chamber and then selectively incorporated at the interface between gold catalyst and the nanowire single crystal. Low growth rates together with rapid switching of the indium source (TMIn) allow for abrupt changes between sections with different compositions, e.g., InAs, InP, or InAsP, along the nanowire with atomically sharp interfaces between them. Figure 1a shows high-angle annular dark-field scanning transmission electron microscope (HAADF-STEM) images of two growth runs for the samples discussed in the current study. The growth direction was from right to left, with the Au particle to the left and the InAs substrate to the right. For sample I, we aimed at growing an asymmetric double dot with dot 1 half the length of dot 2, and for sample II, we aimed at symmetric dot sizes and find good agreement in a subsequent STEM analysis. Within the same growth, the size of the two InAs islands varies less than 5%. Control over the growth of the InP segments is more difficult and was optimized in several iterations. Growing InP on InAs involves a 3.1% lattice mismatch, which means that the first monolayers are grown under tensile strain. As the InP segment increases in length, the strain is relaxed radially, and eventually the growth proceeds unstrained. During the strained growth, the rate for forming a monolayer of InP is lower than for the unstrained situation. If the second InP barrier is grown before the InAs is fully relaxed, the InP grows on partially strained InAs, resulting in a higher initial growth rate. This effect is seen in Figure 1a for sample I, where the barriers surrounding dot 1 are

* Corresponding author. E-mail: Andreas.Fuhrer@ftf.lth.se.

10.1021/nl061913f CCC: $37.00
Published on Web 12/24/2006

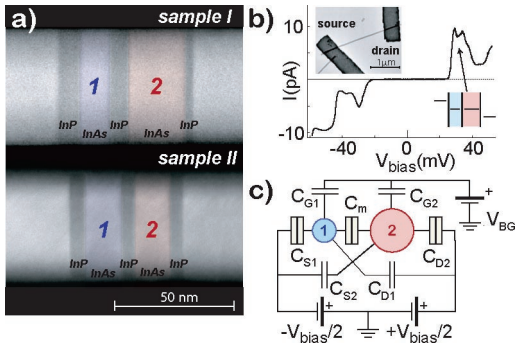

Figure 1. (a) HAADF-STEM micrograph of the InAs/InP nanowire heterostructures. Sample I contains a small InAs dot 1 (blue, l = 11.5 nm), followed by a strongly coupled larger InAs dot 2 (red, l = 22.5 nm) separated by three InP barriers (l = 9.5 nm, 7 nm, 4 nm). Sample II contains two nearly identical dots (l = 15 nm) with nearly identical barriers (l = 5.8 nm). The dimensions may fluctuate from wire to wire depending on the wire diameter (see text). (b) I/V trace showing the clear resonance behavior typical for double dots. The inset shows an SEM image of sample I with two Ni/Au source and drain contacts to which a symmetric bias is applied. (c) Capacitive equivalent circuit used for modeling the data of sample I.

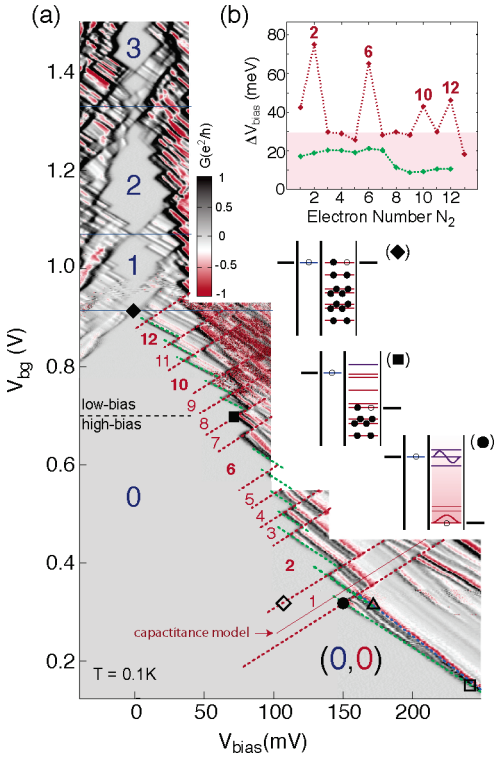

Figure 2. (a) Map of the differential conductance through sample I as a function of the voltage applied to the back gate V_{bg} and the source-drain bias voltage V_{bias}. The number of electrons on the two dots $N_1(N_2)$ are indicated in blue(red) for dot 1(2), respectively. Green dashed lines indicate alignment of the chemical potential μ_1 of dot 1 with that of the source contact μ_s, and red indicates alignment of μ_2 of dot 2 with μ_d in the drain contact. Resonances occur whenever μ_1 and μ_2 align within the bias window, e.g., along the blue dashed line. (b) Addition energies of dot 2 exhibiting magic numbers 2, 6, 10, and 12 compatible with a hard-wall confinement due to the hexagonal cross-section.

grown for the same duration, but the last barrier (on the left) is slightly thicker.

We also find that the first barrier is clearly the thinnest even though it was grown for a 20% longer time than the two subsequent barriers. We believe this is due to a reduced arrival rate of indium precursors present when InP is grown for the first time. Knowing this, we can compensate for both issues by modifying the growth times accordingly, as was done for sample II shown in Figure 1a.

A further optimization parameter is the growth temperature. Sample I is grown at 425 °C, and sample II is grown at 390 °C. At 390 °C almost all of the wires grow perfectly along the *c*-axis in a wurtzite crystal phase (perpendicular to the InAs(111)B substrate surface) throughout the heterostructure. Growth homogeneity at this lower temperature is enormously increased over the growth at 425 °C. We believe that currently the precise control over the barriers is limited by the distribution in wire diameter given by the Au nanoparticle size variation. Within the same growth, we see a clear trend that the thickness of the first InP barrier is larger for thinner wires, with a variability of less than 0.5 nm for wires with the same diameter (45 ± 1 nm). All three barriers in sample II are between 5.8 ± 0.3 nm, demonstrating a high degree of control over the barrier thicknesses.

After growth, nanowires were placed on a degenerately doped Si substrate with a 100 nm thick oxide at its surface acting as a gate dielectric. Ohmic contacts were fabricated using e-beam lithography and subsequent metallization with a 20 nm nickel and 70−100 nm gold layer. A DC bias voltage $\pm V_{bias}/2$ is applied to the source and drain contacts symmetrically, and the current flowing through the device is measured (see inset in Figure 1b). The lengths of the nanowires were typically 3 μm with the InAs/InP heterostructure located in the middle (not visible). For a more detailed description of the device fabrication process and electronic characterization of InAs nanowires, see ref 10 and references therein.

Figure 1b shows an I/V trace for sample I, with the typical resonant behavior indicative of a double dot. At sufficiently large V_{bias}, a resonance peak can occur whenever a level in dot 1 aligns with one in dot 2. Applying a voltage to the back gate tunes both dots simultaneously (see Figure 1c). In a qualitative picture, the small dot 1 is expected to contain fewer electrons than the larger dot 2 and the capacitive coupling of the gate to dot 1 is expected to be smaller than that of dot 2. Tuning the back gate voltage V_{bg} will therefore fill dot 1 more slowly than dot 2, and a more positive V_{bg} will be needed to add the first electron to dot 1. Figure 2 shows a measurement of the differential conductance as a function of both V_{bias} and V_{bg}. The first electron enters dot 1 at around V_{bg} = 0.9 V, where the Coulomb diamonds touch at V_{bias} = 0 V, and then roughly every 0.2 V (blue numbers), an additional electron enters. Superposed on the diamonds of the first dot are kinks in the borderlines (green dashed lines), indicating the more frequent charging of the dot 2. For simplicity, we focus on the region below V_{bg} = 0.9 V from ◆ to □, where the chemical potential in the source contact is aligned to the lowest level in dot 1 (indicated by the green dashed borderlines). The kinks in the green

borderline indicate electrons leaving dot 2 and consequently lowering the chemical potential μ_1 of dot 1. The last electron leaves dot 2 at $V_{bg} \approx 0.32$ V, and a region is reached where no more kinks occur and both dots are empty. The shift ΔV^G_{bias} of the green borderlines, e.g., from ● to △, is indicative of the interdot coupling strength E_{Cm}. The red borderlines mark the alignment of dot 2 with the drain chemical potential μ_d, and their separation ΔV^R_{bias} is indicative of the addition energies $E_{C2} + \Delta E_i$ of dot 2, where E_{C2} is the intradot charging energy of the second dot and ΔE_i is the level spacing. In Figure 2b, both ΔV^G_{bias} and ΔV^R_{bias} are plotted as a function of N_2. ΔV^R_{bias} shows a clear shell structure with magic numbers 2, 6, 10, and 12. For similar single few-electron quantum dots defined using InP/InAs nanowire heterostructures and for a dot length $l < 20$ nm, we found that the lowest longitudinal quantum state (henceforth called *lowest subband*) is occupied up to an electron number $N > 15$.[17] The shell structure is therefore an indication of the symmetry of the radial confinement and the degeneracies of the corresponding levels. The observed sequence of magic numbers is fully consistent with a hexagonal hard-wall confinement potential that can be expected for nanowires grown in the ⟨111⟩B direction but differs from the frequently studied radial symmetric harmonic confinement.[25] As in previous experiments, the addition energy of the first spin pair is slightly larger than that of the other degenerate levels, which is not taken into account in the following analysis.

Increasing V_{bias} beyond the green borderline allows an electron to enter dot 1 and tunnel through the device whenever a level in dot 2 aligns with the lowest state in dot 1, giving rise to pronounced resonances in the current. The slope of these resonance lines (e.g., from △ to □) is different from the green borderline (● to □) because it is the interdot level alignment that is important. For example, for increasing V_{bias} levels, dot 2 will move below those of dot 1, i.e., resonance lines will disappear below the green borderline. The magnitude of the current at these resonance lines changes drastically around ■ in Figure 2a. We attribute this to a transition from resonant tunneling through the lowest subband in dot 2 (◆) to tunneling through the second subband (●), as schematically indicated in the figure. Here we expect a larger tunnel matrix element from the lowest orbital in dot 1 (subband 1) to the lowest orbital in the second subband in dot 2 due to a larger overlap between wavefunctions with similar radial symmetry. This would explain the sudden increase in the current.

The borderlines drawn in Figure 2a are the result of a more quantitative analysis of our data using the capacitance model in Figure 1c and following ref 20. We have extracted the slopes of the three types of borderlines (red, green, resonance line) and ΔV^G_{bias} and ΔV^R_{bias} from the data and used these values as an input to the model in order to determine all the capacitances (see Table 1). In doing so, we distinguish between the low-bias regime ($N_2 \geq 8$) and high-bias regime ($N_2 \leq 7$) due to the two clearly distinct values of ΔV^G_{bias} in the two ranges (see green line in Figure 2b). We generally find that such a constant interaction model can reproduce our data accurately except for the aforementioned addition energy of the second electron to dot 2 (thin red line in Figure 2a), an effect which is related to the reduction of direct Coulomb repulsion for larger electron numbers due to many-body correlations.

Table 1. Capacitances and Coulomb Interaction Energies for the Low-Bias and High-Bias Regime Extracted from the Data Using the Capacitance Model in Figure 1c[a]

capacitance	low-bias [aF]	high-bias [aF]	FE-calculation [aF]
C_{G1}	1.0 ± 0.3	0.8 ± 0.2	
C_{G2}	3.0 ± 0.2	2.8 ± 0.1	
C_{S1}	8.5 ± 5.0	6.9 ± 1.0	7.2
C_{S2}	2.5 ± 0.5	1.4 ± 0.2	1.1
C_{D1}	0.8 ± 0.3	0.9 ± 0.3	1.0
C_{D2}	2.8 ± 0.2	4.6 ± 0.3	4.9
C_m	3.4 ± 1.5	5.7 ± 1.5	3.5
energy	low-bias [meV]	high-bias [meV]	FE-calculation [meV]
E_{C1}	13.2 ± 2.0	13.2 ± 1.0	
E_{C2}	15.8 ± 0.1	13.1 ± 0.1	
E_{Cm}	3.0 ± 1.5	5.2 ± 1.5	

[a] For comparison, the rightmost column shows the values calculated directly from the geometry of the double dot using a finite-element method.

For gate-defined double quantum dots[18−21] $C_{S2} = C_{D1} = 0$, i.e., there is no cross coupling between source and dot 2 or between drain and dot 1. In our case, trying to fit the data to a model with $C_{S2} = C_{D1} = 0$ leads to unphysical negative capacitance values, and we instead allow C_{S2}/C_{S1} and C_{D1}/C_{D2} to vary between 0.1 and 0.3. For this, we find realistic capacitances in the range displayed in Table 1. (For symmetric bias, the expressions for the energy and the chemical potentials of the dots follow directly by replacing $C_S \rightarrow C_{S1} - C_{D1}$ and $C_D \rightarrow C_{D2} - C_{S2}$.) This indicates that, for dot 2, screening of the source contact by dot 1 is not perfect and vice versa. We corroborate this assumption by modeling the capacitance matrix of our geometry in the high-bias limit using a finite-element method. The dots were modeled as two metallic ellipsoids embedded in a freestanding dielectric circular rod with radius $r = 20$ nm and dielectric constant $\epsilon_r = 13$. The size of the ellipsoids, length × width = 6 nm × 18 nm for dot 1 and 10 nm × 14 nm for dot 2, was estimated from a $k \cdot p$ calculation of the wavefunctions in the heterostructure. The centers of the ellipsoids were 19.25 nm apart from each other, and the metallic source(drain) contact was located 14.25 nm (20.3 nm) from the respective ellipsoid center, taking into account both the barriers and a depletion region. The resulting capacitance values show the same trends as the ones obtained from the fit to the data (see Table 1), supporting our capacitance approach. In particular, the magnitude of the cross-coupling capacitances C_{S2} and C_{D1} is confirmed.

Using the measured capacitances for the high-bias regime as an input, we compare the measured current in Figure 3a with that calculated in a rate equation model following ref 22 in Figure 3b. We use one level with a single particle

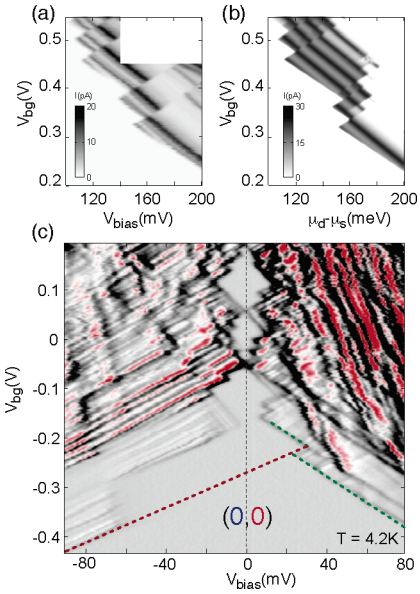

Figure 3. (a) Measured current through sample I in the high-bias regime showing the resonance line positions for interdot alignment between m_1 and m_2. (b) Current in the same range as (a), calculated using a rate equation model together with the capacitances extracted in Table 1. (c) Map of the differential conductance through sample II as a function V_{bg} and V_{bias}.

energy of 97 μeV in the left dot with a coupling $\Gamma_L = 0.05$ μeV to the source contact. In the right dot, we consider three levels in the lowest subband at energies 13, 42, and 42 μeV, coupling $\Gamma_R = 10$ μeV to the drain contact and tunnel coupling $\Gamma = 20$ μeV as well as seven levels in the second subband, with equal spacing between 146 and 167 μeV, $\Gamma_R = 100$ μeV, and $\Gamma = 50$ μeV. All levels are assumed to be spin degenerate. Here we refrained from a detailed fit for the location, height, and width of the resonances lines in order to avoid too many fitting parameters besides the capacitances discussed above. We find good agreement of the overall behavior except for the shifts in the resonance lines when charging dot 2. These shifts are too large in the calculation, indicating that the charging energy for the second subband is smaller than the charging energy for the first subband. This feature is expected but goes beyond a capacitance matrix model.

Figure 3c shows the same type of measurement for sample II where dot 1 and dot 2 were designed to have the same size. Electronically, dot 2 is again slightly larger, but the asymmetry between the dots is strongly reduced such that a maximum of two electrons fill dot 2 before the first electron enters dot 1. On this scale, the asymmetry between the two dots is found to vary from wire to wire. On the one hand, this can be explained as outlined above due to differences between wires within the same growth run. On the other hand, we also observe variability on the scale of a single charging energy E_{C2} from cooldown to cooldown, indicating that either in the SiO_2 gate dielectric or at the surface of the nanowire, charge traps modify the electronic environment of the double dots. This problem has to be addressed in the future, e.g., using an epitaxially grown shell in order to achieve reproducibility beyond the single electron limit.

In conclusion, we have demonstrated the fabrication of high-quality double quantum dot structures that can be described on a semiquantitative basis using a capacitance and rate equation model. Similar data has been obtained in self-assembled vertically aligned InAs quantum dots.[23] While control over dot size and electron number is likely to be difficult in the case of the self-assembled dots, we have demonstrated that a high degree of control is possible for nanowire heterostructure-based double-dot systems. We consider such control over the electronic structure of double quantum dots to be the first step toward designing advanced electronic heterostructure devices using semiconducting nanowires.

Acknowledgment. This work was supported by the Swedish Foundation for Strategic Research (SSF), the Swedish Research Council (VR), the Office of Naval Research (ONR), and the Swiss Science Foundation (Schweizerischer Nationalfonds).

References

(1) Avouris, P.; Hertel, T.; Martel, R.; Schmidt, T.; Shea, H. Walkup, R. *Appl. Surf. Sci.* **1999**, *141*, 201.
(2) McEuen, P. L.; Fuhrer, M. S.; Park, H. *IEEE Trans. Nanotechnol.* **2002**, *1*, 78.
(3) Samuelson, L.; Thelander, C.; Björk, M. T.; Borgström, M.; Deppert, K.; Dick, K. A.; Hansen, A. E.; Martensson, T.; Panev, N.; Persson, A. I.; Seifert, W.; Skold, N.; Larsson, M. W.; Wallenberg, L. R. *Physica. E* **2002**, 22.
(4) Yang, P.; Wu, Y.; Fan, R. *Int. J. Nanosci.* **2002**, *1*, 1.
(5) Xiang, J.; Lu, W.; Wu, Y.; Yan, H.; Lieber, C. M. *Nature* **2006**, *441*, 1038.
(6) Wang, D.; Wang, Q.; Javey, A.; Tu, R.; Dai, H.; Kim, H.; McIntyre, P. C.; Krishnamohan, T.; Saraswat, K. C. *Appl. Phys. Lett.* **2003**, *83*, 2432.
(7) Haraguchi, K.; Katsuyama, T.; Hiruma, K.; Ogawa, K. *Appl. Phys. Lett.* **1991**, *60*, 745.
(8) Bryllert, T.; Wernersson, L.-E.; Jensen, L. E.; Samuelson, L. *IEEE Electron Device Lett.* **2006**, *27*, 323.
(9) Martensson, T.; Borgstrom, M.; Seifert, W.; Ohlsson, B. J.; Samuelson, L. *Nanotechnology* **2003**, *14*, 1255.
(10) Björk, M. T.; Thelander, C.; Hansen, A. E.; Jensen, L. E.; Larsson, M. W.; Wallenberg, L. R.; Samuelson, L. *Nano Lett.* **2004**, *4*, 1621.
(11) Persson, A. I.; Björk, M. T.; Jeppeson, S.; Wagner, J. B.; Wallenberg, L. R.; Samuelson, L. *Nano Lett.* **2006**, *6*, 403.
(12) Yang, C.; Zhaohui, Z.; Lieber, C. M. *Science* **2005**, *310*, 1304.
(13) Lauhon, L. J.; Gudiksen, M. S.; Wang, D.; Lieber, C. M. *Nature* **2006**, *420*, 57.
(14) Sköld, N.; Karlsson, L. S.; Larsson, M. W.; Pistol, M. E.; Seifert, W.; Trägårdh, J.; Samuelson, L. *Nano Lett.* **2005**, 5, 1943.
(15) Hiruma, K.; Murakoshi, H.; Katsuyama, T. *J. Cryst. Growth* **1996**, *163*, 226.
(16) Thelander, C.; Nilsson, H. A.; Jensen, L. E.; Samuelson, L. *Nano Lett.* **2005**, *5*, 635.
(17) Björk, M. T.; Fuhrer, A.; Hansen, A. E.; Larsson, M. W.; Jensen, L. E.; Samuelson, L. *Phys. Rev. B* **2005**, *72*, 201307(R).
(18) van der Wiel, W. G.; De Franceschi, S.; Elzerman, J. M.; Fujisawa, T.; Tarucha, S.; Kouwenhoven, L. P. *Rev. Mod. Phys.* **2003**, *75*, 1.
(19) Biercuk, M. J.; Garaj, S.; Mason, N.; Chow, J. M.; Marcus, C. M. *Nano Lett.* **2005**, *5*, 126.
(20) Sapmaz, S.; Meyer, C.; Beliczynski, P.; Jarillo-Herrero, P.; Kouwenhoven, L. P. *Nano Lett.* **2006**, *6*, 1350.
(21) Fasth, C.; Fuhrer, A.; Björk, M. T.; Samuelson, L. *Nano Lett.* **2005**, *5*, 1487.
(22) Sprekeler, H.; Kiesslich, G.; Wacker, A.; Schöll, E. *Phys. Rev. B* **2004**, *69*, 125328.
(23) Ota, T.; Ono, K.; Stopa, M.; Hatano, T.; Tarucha, S.; Song, H. Z.; Nakata, Y.; Miyazawa, T.; Ohshima, T.; Yokoyama, N. *Phys. Rev. Lett.* **2004**, *93*, 066801.
(24) Jensen, L. E.; Björk, M. T.; Jeppesen, S.; Persson, A. I.; Ohlsson, B. J.; Samuelson, L. *Nano Lett.* **2004**, *4*, 1961.
(25) Reimann, S. M.; Manninen, M. *Rev. Mod. Phys.* **2002**, *74*, 1283.

NL061913F